

# Gravitational Clustering in Redshift Space: Non-Gaussian Tail of the Cosmological Density Distribution Function

J. S. Bagla<sup>1</sup> and Suryadeep Ray<sup>2</sup>

<sup>1</sup> Harish-Chandra Research Institute, Chhatnag Road, Jhusi, Allahabad 211019, India.

<sup>2</sup> Inter-University Centre for Astronomy and Astrophysics, Post Bag 4, Ganeshkhind, Pune 411007, India

E-mail: <sup>1</sup> jasjeet@hri.res.in, <sup>2</sup> surya@iucaa.ernet.in

6 May 2019

## ABSTRACT

We study the non-Gaussian tail of the probability distribution function of density in cosmological N-Body simulations for a variety of initial conditions. We compare the behaviour of the non-Gaussian tail in the real space with that in the redshift space. The form of the PDF in redshift space is of great significance as galaxy surveys probe this and not the real space analogue predicted using theoretical models. We model the non-Gaussian tail using the halo model. In the weakly non-linear regime the moments of counts in cells in the redshift space approach the values expected from perturbation theory for moments in real space. We show that redshift space distortions in the non-linear regime dominate over signatures of initial conditions or the cosmological background. We illustrate this using Skewness and higher moments of counts in cells, as well as using the form of the non-Gaussian tail of the distribution function. We find that at scales smaller than the scale of non-linearity the differences in Skewness, etc. for different models are very small compared to the corresponding differences in real space. We show that bias also leads to smaller values of higher moments, but the redshift space distortions are typically the dominant effect.

**Key words:** gravitation – cosmology : theory, dark matter, large scale structure of the universe

## 1 INTRODUCTION

Large scale structures are thought to have formed by gravitational amplification of small perturbations (Peebles 1980; Peacock 1999; Padmanabhan 2002; Bernardeau et al. 2002). Galaxies are believed to form when gas in highly over dense haloes cools and collapses to form stars in large numbers (Hoyle 1953; Rees & Ostriker 1977; Silk 1977; Binney 1977). Evolution of density perturbations due to gravitational interaction in a cosmological setting is, therefore, the key process for the study of galaxy clustering and its evolution. It is also one of the most important processes in formation and evolution of galaxies. The basic equations for evolution of density perturbations are well known (Peebles 1974) and are easy to solve when the amplitude of perturbations is small. Once the amplitude of perturbations at relevant scales becomes large, the perturbation becomes non-linear and the coupling with perturbations at other scales cannot be ignored. The equation for evolution of density perturbations cannot be solved for generic perturbations in the non-linear regime. One can use quasi-linear approximations for studying mildly non-linear perturbations (Zel'Dovich 1970; Gurbatov, Saichev, & Shandarin 1989; Shandarin & Zeldovich 1989; Matarrese et al. 1992; Brainerd, Scherrer, & Villumsen 1993; Bagla & Padmanabhan 1994; Sahni & Coles 1995; Hui & Bertschinger 1996; Bernardeau et al. 2002). Statistical approximations and scaling relations can be used if a limited amount of information is suf-

ficient (Davis & Peebles 1977; Hamilton et al. 1991; Jain, Mo, & White 1995; Kanekar 2000; Ma 1998; Nityananda & Padmanabhan 1994; Padmanabhan et al. 1996; Padmanabhan 1996; Peacock & Dodds 1996; Smith et al. 2003). In general, however, we require cosmological N-Body simulations (Bertschinger 1998; Bagla 2005; Bagla and Padmanabhan 1997b) to follow the detailed evolution of the system.

The initial density distribution is often assumed to be a Gaussian random field (Bardeen et al. 1986). The power spectrum or the two point correlation function is sufficient for describing such a field. Gravitational clustering leads to departures from a strictly Gaussian field and we need to specify the full hierarchy of  $n$ -point correlation functions in order to provide a complete description of the density field at late times (Peebles 1980; Bernardeau et al. 2002). The distribution of matter represented by galaxies, etc. is strongly non-Gaussian at small scales and hence it is necessary to measure higher order moments of the galaxy distribution, if not the full probability distribution function.

Redshift surveys give us information about the distribution of galaxies in redshift space. For a given galaxy, the redshift is a combination of information about the radial distance and the radial component of the peculiar velocity. Although it is possible to construct distribution of galaxies in real space at large scales, the techniques used are not suitable for recovering information at small scales (Bertschinger & Dekel 1989; Dekel, Bertschinger, & Faber

## 2 Bagla and Ray

1990; Nusser & Dekel 1992; Croft & Gaztanaga 1997; Buchert & Dominguez 1998; Narayanan & Weinberg 1998; Narayanan & Croft 1999; Taylor & Valentine 1999; Monaco & Efstathiou 1999; Whiting 2000; Frisch et al. 2002; Branchini, Eldar, & Nusser 2002; Brenier et al. 2003; Mohayaee et al. 2003; Mohayaee, Tully, & Frisch 2004). Therefore we are confined to studying the galaxy distribution in redshift space at small scales, and hence it is important to understand the effect of redshift space distortions on the distribution of galaxies.

It is well known that galaxies do not trace the matter distribution, i.e., the galaxy distribution is biased. This is reflected in the clustering properties of galaxies which should differ from the clustering of matter, e.g., the correlation function and the reduced moments are expected to be different for galaxies. It is known that highly over dense regions cluster much more strongly than the overall distribution of matter, and the peak picture provides a natural explanation for this (Kaiser 1984). This can explain the large two point correlation function of galaxies at high redshifts, e.g. see Brainerd & Villumsen (1994); Bagla (1998a). It can be combined with other inputs to develop an understanding of the evolution of galaxy clustering (Mo & White 1996; Fry 1996; Matarrese et al. 1997; Bagla 1998b; Roukema et al. 1999).

The clustering of galaxies depends on the environment, galaxy type and other factors that are relevant for galaxy formation and evolution. It is difficult to codify the physics of galaxy formation in simple terms and hence these aspects are modelled in terms of a stochastic bias (Tegmark & Peebles 1998; Dekel & Lahav 1999; Sheth, Mo, & Tormen 2001; Sheth & Tormen 2004).

In this paper we study the counts in cells using N-Body simulations. We model the probability distribution function in redshift space using the halo model. We also study the effect of bias on moments of counts in cells, both in real and redshift space.

The paper is organised as follows: we review some basics of gravitational clustering in §2. In §3 we discuss the simulations used in this work and also present the key results. We conclude with a discussion (§4).

### 2 GRAVITATIONAL CLUSTERING

The evolution of density perturbations can be studied in the Newtonian limit at sufficiently small scales for non-relativistic matter. Indeed, it has been shown that the Newtonian analysis gives the correct solution up to at least the third order for cold dark matter models even when a finite cosmological constant is present (Hwang & Noh 2005). Thus the Newtonian limit can be used with confidence at scales sufficiently smaller than the Hubble radius. Evolution of perturbations can then be described by the following equations.

$$\begin{aligned} \ddot{\mathbf{x}}_i + 2\frac{\dot{a}}{a}\dot{\mathbf{x}}_i &= -\frac{1}{a^2}\nabla_i\varphi \\ \nabla^2\varphi = 4\pi G a^2(\rho - \bar{\rho}) &= \frac{3}{2}H_0^2\Omega_{nr}\frac{\delta}{a} \\ \rho(\mathbf{x}) &= \sum_i m_i \delta_D(\mathbf{x} - \mathbf{x}_i) \end{aligned} \quad (1)$$

It is assumed that the density field is generated by a distribution of particles, each of mass  $m_i$  and comoving position  $\mathbf{x}_i$ .  $H_0$  is the present value of Hubble constant,  $\Omega_{nr}$  is the present density parameter for non-relativistic matter and  $a$  is the scale factor. Density contrast  $\delta = (\rho - \bar{\rho})/\bar{\rho}$ , where  $\bar{\rho}$  is the average density. It is clear from these equations that over dense regions ( $\delta > 0$ ) grow by pulling in matter from surrounding regions while under dense re-

gions ( $\delta < 0$ ) become more under dense and start to occupy larger volume.

It can be shown that gravitational instability leads to formation of highly dense haloes that are in virial equilibrium or close to it (Peebles 1974; Peebles 1980). These haloes are the dominant structures at late times and several properties of the density field can be deduced by considering the haloes to be the basic unit (Mo & White 1996; Mo, Jing, & White 1997; Cooray & Sheth 2002). This approach is known as the halo model.

#### 2.1 Moments of Counts in Cells

Given a distribution of points, estimation of  $n$ -point correlation functions is a very difficult task as this computation requires  $\mathcal{O}(N^n)$  floating point operations for a set of  $N$  particles. One can, however, compute the moments of counts in cells and recover some information about  $n$ -point correlation functions (Peebles 1980; Colombi, Bouchet, & Schaeffer 1995). In this method, we distribute a large number of cells in the volume containing the distribution of points and count the number of particles in each cell. The count probability distribution function (CPDF) is a function of the cell size and the count, of course. The CPDF contains full information about the distribution of points. It can be used to estimate the moments, which in turn are related to the  $n$ -point correlation functions. The number of operations required for calculating the CPDF at a given scale is  $\mathcal{O}(N\bar{n}V)$ , where  $\bar{n}$  is the number density of particles and  $V$  is the volume of each cell. This reduction in the computation required is remarkable but there is also a reduction in the amount of information we can recover about the  $n$ -point correlation functions. To illustrate this, we give some basic definitions here:

$$\begin{aligned} \bar{N}_c &= \langle N_c \rangle = \bar{n}V \\ \mu_j &= \langle (N_c - \bar{N}_c)^j \rangle \quad ; \quad j = 2, 3, \dots \end{aligned} \quad (2)$$

where  $N_c$  is the number of particles in a cell and  $\bar{N}_c$  is its average value for cells of a given size.  $\mu_j$  are moments of the CPDF about the average and these can be related to  $n$ -point correlation functions.

$$\begin{aligned} \frac{\mu_2}{\bar{N}_c^2} &= \bar{\xi}(r) + \frac{1}{\bar{N}_c} \\ \frac{\mu_3}{\bar{N}_c^3} &= \bar{\zeta}(r) + 3\frac{\bar{\xi}(r)}{\bar{N}_c} + \frac{1}{\bar{N}_c^2} \\ \frac{\mu_4}{\bar{N}_c^4} &= \bar{\eta}(r) + 3\bar{\xi}^2(r) + 6\frac{\bar{\zeta}(r)}{\bar{N}_c} \\ &\quad + \left(\frac{7}{\bar{N}_c^2} + \frac{6}{\bar{N}_c}\right)\bar{\xi}(r) + \frac{3}{\bar{N}_c^2} - \frac{4}{\bar{N}_c^3} \end{aligned} \quad (3)$$

Here,  $\bar{\xi}$  is the mean two point correlation function,  $\bar{\zeta}$  is the mean three point correlation function and  $\bar{\eta}$  is the corresponding four point function (Peebles 1980). Note that lower order correlation functions contribute a non-trivial amount to higher order moments and  $\bar{\xi}$ ,  $\bar{\zeta}$ ,  $\bar{\eta}$ , etc. correspond to the irreducible part of the  $n$ th order correlation function. These expressions include corrections for shot noise. From here, we can define reduced moments as:

$$\begin{aligned} S_3 &= \frac{\bar{\zeta}(r)}{\bar{\xi}^2(r)} \\ S_4 &= \frac{\bar{\eta}(r)}{\bar{\xi}^3(r)} \end{aligned} \quad (4)$$

Here,  $S_3$  is the Skewness and  $S_4$  is Kurtosis. These reduced moments are expected to vanish in the linear regime for Gaussian ini-

tial conditions. Gravitational instability introduces mode coupling and this leads to generation of non-Gaussian features. Perturbation theory can be used to estimate the values of Skewness and other reduced moments in the weakly non-linear regime ( $\bar{\xi} \ll 1$ ). For power law models in an Einstein-de Sitter universe, the reduced moments do not depend on scale in this regime (Peebles 1980; Colombi, Bouchet, & Hernquist 1996).

$$\begin{aligned} S_3 &= \frac{34}{7} - (n+3) \\ S_4 &= \frac{60712}{1323} - \frac{62}{3}(n+3) + \frac{7}{3}(n+3)^3 \end{aligned} \quad (5)$$

here  $n$  is the index of the initial power spectrum of density perturbations. It is difficult to obtain a direct solution in the strongly non-linear regime. Stable clustering and hierarchical clustering predict a constant asymptotic value (Davis & Peebles 1977; Colombi, Bouchet, & Hernquist 1996)

$$S_3 = \frac{9}{n+3} \quad (6)$$

Therefore we expect  $S_3$  (and also  $S_4$ ) to grow from their value in the weakly non-linear regime (Eqn.(5)) to a larger value in the extremely non-linear regime (Eqn.(6)). The increase is larger for indices with small  $n+3$ , as is clear from eqn.(6). Small departures from the stable clustering hypothesis have been seen in simulations (Colombi, Bouchet, & Hernquist 1996).

## 2.2 Redshift Space Distortions

Redshift surveys of galaxies give us information about the location of galaxies in the redshift space. Combination of the peculiar motion of galaxies and cosmological expansion determines the redshift of a galaxy and as a result the location in redshift space is different from the location of the galaxy in real space. This affects the estimated position along the line of sight and does not change the location transverse to the line of sight. Thus redshift space distortions introduce anisotropy in the distribution of galaxies, even if there is no statistical anisotropy in the galaxy distribution in real space. On small scales, the random motions in virialised haloes stretch these into radially elongated *fingers-of-god*. Even though the effect originates from random motions in compact clusters, it is relevant at scales as much as twenty times the size of a typical cluster. On very large scales, infall due to gravitational clustering compresses over dense regions along the line of sight. The compression is a function of infall velocities, and these depend on the density parameter of non-relativistic matter. This compression leads to an amplification of power spectrum and correlation function at these scales (Kaiser 1987). For galaxies and other tracers of the matter distribution, the compression also depends on bias, e.g., see Dekel & Lahav (1999).

The halo model (Mo & White 1996; Mo, Jing, & White 1997; Cooray & Sheth 2002) has been used to model the effect of redshift space distortions on the non-linear power spectrum at scales where the dominant contribution is from random motions in virialised haloes (White 2001; Seljak 2001). At small scales, where the coherent motion of galaxies due to large scale flows (Kaiser 1987) can be ignored, the relation between the observed density in real space  $\rho^{(r)}(\mathbf{r})$  and that in redshift space  $\rho^{(s)}(\mathbf{s})$  can be expressed as follows (Matsubara 1994).

$$\rho^{(s)}(\mathbf{s}) = \int_{-\infty}^{+\infty} dv f_{\sigma}(v) \rho^{(r)}(\mathbf{s} + H_0^{-1} v \hat{\mathbf{s}}) \quad (7)$$

where  $f_{\sigma}(v)$  is the distribution function of peculiar velocities and

$$\int_{-\infty}^{+\infty} dv f_{\sigma}(v) = 1 \quad (8)$$

In these equations  $H_0$  is, as before, the present value of Hubble constant. The observer is presumed to be at the origin of the coordinates and  $\hat{\mathbf{s}} \equiv \mathbf{s}/|\mathbf{s}|$  is the unit vector towards any location  $\mathbf{s}$  in the redshift space.

Within the formalism of the halo model the amplitude of the power spectrum at small scales (large  $k$ ) is dominated by halo profiles and virial motions within haloes act to reduce the amplitude of the power in redshift space. If one assumes that in real space the haloes are isotropic, virialised and approximately isothermal with 1D velocity dispersion  $\sigma$ , then the peculiar motions *within* a halo add a Gaussian noise to the redshift space radial coordinate (White 2001) in Fourier space.

$$\rho_k^{(s)} = \rho_k^{(r)} \exp \left[ -\frac{(kH_0^{-1}\sigma\mu)^2}{2} \right], \quad (9)$$

where  $\mu = \hat{\mathbf{r}} \cdot \hat{\mathbf{k}}$ . The effect of redshift space distortions on the power spectrum can be calculated by integrating over  $\mu$  (White 2001). However, we are interested in higher moments and the anisotropic halo profile is required for an accurate description.

## 3 N-BODY SIMULATIONS

In the present work, we study the moments of counts in cells in N-Body simulations. We compute  $\bar{\xi}$ ,  $S_3$  and  $S_4$  for a variety of initial conditions in real space as well as redshift space. We primarily concentrate on simulations of power law models in an Einstein-de Sitter background Universe ( $\Omega_m = 1.0$ ):

$$P(k) = Ak^n \quad (10)$$

We ran simulations of power-law models with index  $n = -2, -1$  and 0. These were normalised such that linear fluctuations at the scale of 8 grid lengths were unity when the scale factor  $a = 1$ . Power law models do not have any intrinsic scale except for the scale of non-linearity introduced by gravity. Self similar evolution of indicators of clustering is a good check for the accuracy of simulations for such models.

We also simulated the  $\Lambda$ CDM model with  $\Omega_b = 0.05$ ,  $\Omega_{dm} = 0.25$ ,  $\Omega_{tot} = 1.0$ ,  $h = 0.7$  and  $n = 1.0$ , where  $h$  is the dimensionless Hubble parameter and  $n$  is the primordial spectral index. The power spectrum was normalised by choosing  $\sigma_8(z=0) = 1$ .

The parallel TreePM method (Bagla 2002; Bagla & Ray 2003; Ray & Bagla 2004) was used for all simulations. We assumed that the particles have a finite size given by a spline kernel (Springel, Yoshida, & White 2001) to obtain a softened force. The softening length used is listed in table 1 along with other parameters of simulations used here.

We also study clustering properties of over dense regions as this approximates the distribution of galaxies, though it is more appropriate to work with a model for occupation number for a more refined study (Benson 2001). We identify high density regions in our simulations by using a density cutoff. We compute the Lagrangian density of particles in a given simulation using a top-hat kernel with a radius equal to the distance to an  $n$ th neighbour with  $n \simeq 10$ . We then retain particles in regions with density greater than a given threshold.

Model	$N_p$	$N_{cell}$	$L_{box}$	$\epsilon$	$r_{nl}$
Power Law $n = -2.0$	$256^3$	$256^3$	256 (grid units)	0.4 (grid units)	5.0 (grid units)
Power Law $n = -1.5$	$256^3$	$256^3$	256 (grid units)	0.4 (grid units)	8.0 (grid units)
Power Law $n = -1.0$	$256^3$	$256^3$	256 (grid units)	0.4 (grid units)	8.0 (grid units)
Power Law $n = -0.5$	$256^3$	$256^3$	256 (grid units)	0.4 (grid units)	9.0 (grid units)
Power Law $n = 0.0$	$256^3$	$256^3$	256 (grid units)	0.4 (grid units)	10.0 (grid units)
$\Lambda$ CDM	$256^3$	$256^3$	$200h^{-1}\text{Mpc}$	$0.47h^{-1}\text{Mpc}$	$8.0h^{-1}\text{Mpc}$

**Table 1.** This table lists the fixable parameters of the N-Body simulations we have used. All the simulations were done using the TreePM code; the detailed configuration is described in Bagla & Ray (2003). The first column lists the model used in generating the initial conditions for a simulation, the second column lists the number of particles in the simulation, the third column the size of the cubic grid used within the simulation volume to compute Fourier transforms for the long range part of the force of gravitational interaction, the fourth column the length of a side of the simulation box in relevant units and the last column the softening length for force in the same units. A *grid unit* here is defined as the length of the side of the smallest cell in the grid within the simulation box. The last column lists the largest scale of non-linearity  $r_{nl}$  for a given model that we have used for our analysis.

We use power law models as the requirement of scale invariant evolution is a powerful constraint and it can be used to ensure that the simulations do not suffer from any serious defect. This is a particularly useful approach for models with a lot of power at large scales as in this case the effects of a finite box size can be important (Bagla & Ray 2005; Bagla & Prasad 2006). We find that in the simulations we have used here, scale invariance is satisfied up to the last epoch used here for the second moment.

In order to calculate the CPDF, we used a large number of uniformly distributed spherical cells. The number of cells varied from  $10^8$  for the smallest cells to  $1.6 \times 10^7$  for the largest cells. Radii of cells were varied in the range 0.6 to 20 grid lengths. As the largest cell size used is much smaller than the simulation box size, cosmic variance is not a concern.

We first verify the perturbative prediction for  $S_3$  in the weakly non-linear regime, and also check for any variations in moments in this regime as we go to redshift space. Figure 1 shows  $S_3$  as a function of the spectral index  $n$  for power law models. This value of  $S_3$  is the average obtained from scales where  $0.1 \leq \xi \leq 0.2$ . We do not expect the values of  $S_3$  to deviate too strongly from the perturbative predictions at these scales. As seen in the figure, the values of  $S_3$  are close to the predictions given in Eqn.(5). The values of  $S_3$  encountered in redshift space are generally smaller, mainly due to the fingers of god effect. For analytical predictions of Skewness in redshift space see Taylor & Watts (2000); Watts & Taylor (2001).

We also study the variation of  $S_3$  in the strongly non-linear regime. The lower panel of Figure 1 shows  $S_3$  as a function of  $n$  for  $\xi \geq 30$ . Also shown is the variation expected from the stable clustering hypothesis (Eqn.(6)). As stable clustering is expected only at much higher levels of non-linearity, we expect these simulations to under-estimate  $S_3$  as compared to the analytical prediction. The simulations and the analytical predictions are consistent with each other at this level, except  $n = -2$  where we believe the effects of a finite box size are starting to manifest themselves (Bagla & Ray 2005; Bagla & Prasad 2006). The real test of the stable clustering hypothesis requires carrying out this comparison at  $\xi \gg 100$  and we have not reached such non-linearities in the simulations used here.

Having verified known results about the moments, we proceed with a discussion of the non-Gaussian tail of the CPDF. We start with a comparison of the tail of CPDF with an analytical calcu-

lations done with the halo model. Figure 2 shows the CPDF for the  $n = 0$  and  $n = -2$  power law models for a small cell-size ( $l = 0.6$  grid length) in both real and redshift space. We find that the tail of the CPDF in redshift space falls off much more sharply as compared to the corresponding tail of CPDF in real space. Partly due to the different slope, the CPDF in redshift space is larger than the CPDF in real space at intermediate densities. The basic features are similar for  $n = 0$  and  $n = -2$  and this suggests that redshift space distortions may be responsible for the key features rather than any power spectrum dependent quantity. The differences in the two panels here may be attributed to the different scale of non-linearity, as this results in different sizes for the most massive haloes whereas the cell size used here is the same for both the models.

### 3.1 The Non-Gaussian Tail

Higher moments are sensitive to the form of the non-Gaussian tail of the CPDF and hence we need to model the contribution of central parts of haloes to the CPDF. We model the non-Gaussian tail of the CPDF in redshift space using the halo model. We follow the approach used by Colombi et al. (1994); Taruya, Hamana, & Kayo (2003) for this, and extend their formalism to redshift space.

Let us assume that in real space the haloes are spherical with a central profile that can be approximated as

$$\rho^{(r)}(r) = \rho_c \left( \frac{r}{r_c} \right)^{-\alpha} \quad (11)$$

As the density field is represented by point particles, the number density of these particles is proportional to the density  $\rho$ . If the cell size is much smaller than characteristic scales of typical haloes then the tail of the CPDF can be estimated approximately by computing the volume occupied by regions with density greater than a threshold. As long as the effects of a finite number of particles are not important, the CPDF is expected to have the form  $P_N(R) \propto N^{-3/\alpha-1}$ , with  $R$  being the cell size (Colombi et al. 1994). Use of a finite sized cell implies smoothing of the density field (Taruya, Hamana, & Kayo 2003), therefore the highest density sampled in a given halo is finite even if the actual density profile is singular. The smoothing also implies that there is a minimum halo mass and only haloes more massive than this minimum contribute to the non-Gaussian tail, though this cutoff is rarely of much significance as much of the contribution to the tail of the CPDF comes from most massive haloes. To generalise the calculation of the form

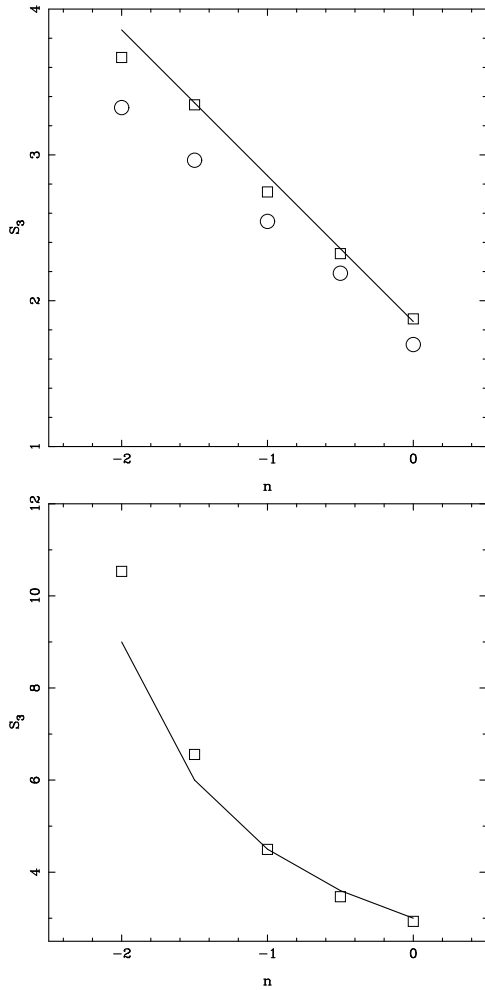


**Figure 1.**  $S_3$  has been plotted for power law models as a function of the power law index  $n$  in the weakly non-linear regime for both real and redshift space in the upper panel. For a given  $n$ , we have plotted the average  $S_3$  with  $0.1 \leq \xi \leq 0.2$ . We used data from several epochs for each model. The average  $S_3$  is plotted as a function of  $n$ . The rectangles correspond to the value of  $S_3$  in real space, whereas the circles show the same in redshift space. The full line represents the predicted values from perturbation theory (refer to the text for further details). In the lower panel  $S_3$  has been plotted as a function of  $n$  in real space in the non-linear regime ( $\xi \geq 30$ ). The curve shows the predicted variation in the stable clustering hypothesis.

of the non-Gaussian tail to haloes in redshift space, we note that in this case the density profile cannot be assumed to be isotropic. We first compute the density profile in redshift space (Eqn.7) and then compute the volume ( $V(> \rho)$ ) occupied by regions with density above a threshold. We may approximate Eqn.(7) as:

$$\rho^{(s)}(\mathbf{s}) = \int_{-\infty}^{+\infty} dv f_{\sigma}(v) \rho^{(r)}(\mathbf{s} + H_0^{-1} v \hat{\mathbf{s}})$$

$$\simeq \frac{1}{2\sigma} \int_{-\sigma}^{\sigma} dv \rho^{(r)}(\mathbf{s} + H_0^{-1} v \hat{\mathbf{s}}) . \quad (12)$$

$$(13)$$

In this approximation, the effect of redshift space distortions leads to a redistribution of the mass contained in an infinitesimally thin

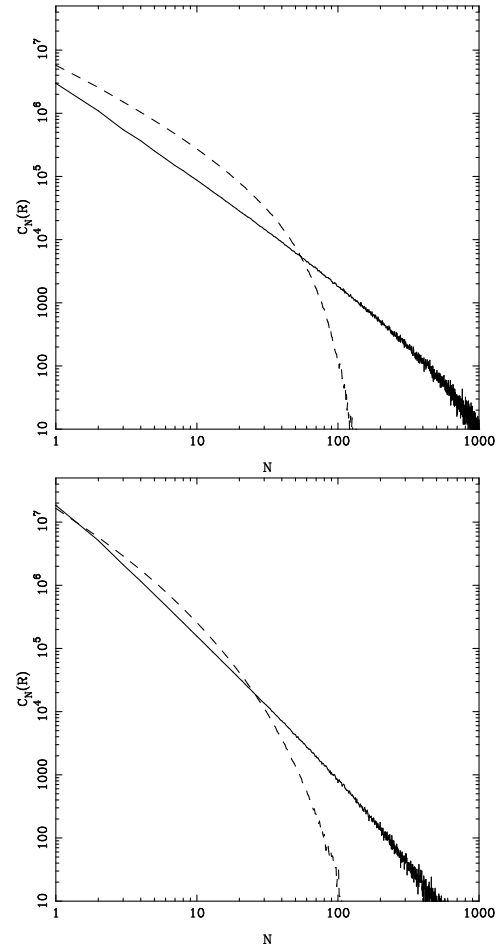


**Figure 2.** The distribution of counts  $C_N$  in cells is shown for power law models with  $n = 0$  (top panel) and  $n = -2$  (lower panel). These are for cell of size of  $R = 0.6$  grid lengths. This scale is smaller than the virial radius of largest haloes in the simulations. Solid line shows the counts in real space and the dashed line shows the counts in redshift space. The plots were made using data for the highest  $r_{nl}$  listed in table 1 for the corresponding model.

cylinder of length  $2\sigma H_0^{-1}$  along the line of sight<sup>1</sup>. Such a redistribution clearly leads to a smaller central density and therefore the maximum density in a small ( $R \ll r_{vir}$ ) finite sized cell in redshift space is much smaller than its counterpart in real space. However, the volume occupied by regions with this maximum density is much larger and hence a large number of cells sample densities close to the theoretical maximum. Therefore in redshift space, the CPDF should be steeper than its real space counterpart. This is mainly because the volume occupied by densities close to the theoretical maximum is much larger in redshift space than the corresponding volume in real space.

As an aside, we note that the density profile in the transverse direction ( $s_{\perp}$ ) is shallower than the real space density profile. The difference in slope near the centre is unity for power law models.

<sup>1</sup> We make this approximation in order to understand the qualitative aspects of density profile in redshift space and the corresponding features in the CPDF; the first of the two equations given here is used for the detailed calculations that follow. Further, we use the NFW profile for our calculations and do not restrict ourselves to power law profiles.

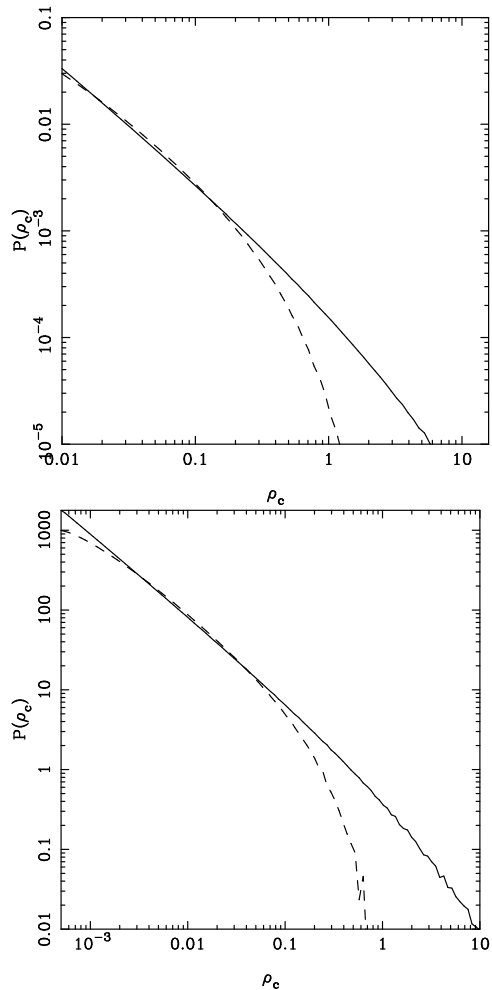


**Figure 3.** The upper panel shows the unnormalised probability distribution function for a NFW halo plotted as a function of average density in the cell  $\rho_c$ . A cell size of  $0.01 r_{vir}$ , and a uniform  $\sigma$  evaluated at the virial radius was used here. Density is shown in units of the density at the virial radius. The solid line shows the distribution function in real space and the dashed line is for the distribution function in redshift space. This brings out the key feature of a cutoff in the probability distribution in redshift space. In contrast, the real space distribution function tapers off at much higher densities. The lower panel shows the volume occupied by regions with density  $\rho_c$  as a function of  $\rho_c$  for the  $n = -2$  power law model. Both the density and volume are in arbitrary but self consistent units here. The volume is equivalent to unnormalised probability. The solid line is for real space and the dashed line for redshift space. These have been computed using the halo model with the Press-Schechter mass function and assuming a NFW profile. Refer to the text for further details.

This dictates the shape of the power spectrum at wave numbers that are much larger than  $1/(\sigma H_0^{-1})$  and  $1/r_{vir}$ .

Figure 3 shows the (unnormalised) probability distribution function for an NFW halo computed using the approach followed by Taruya, Hamana, & Kayo (2003) that we have outlined above. The probability is proportional to the volume occupied by regions with the given density. This figure brings out the key feature of a smaller cutoff in the probability distribution in redshift space. As expected from the approximate treatment given above, the slope of the non-Gaussian tail is also different: probability falls off very rapidly near the maximum density. The real to redshift space mapping also enhances the probability at densities below the maximum

density in real space. This analysis is for a single halo and the net effect on the CPDF is calculated by convolving the mass function with the density profile.

$$P(> N) \sim P(> \rho) \propto \int dM n(M) V(> \rho; M) \quad (14)$$

here,  $V(> \rho; M)$  is the volume occupied by regions with density greater than  $\rho$  in haloes of mass  $M$ . The number density of haloes with mass between  $M$  and  $M + dM$  is given by  $n(M) dM$ . An analysis with finite sized cells requires a smoothing of the density profile; however we find that we do not require significant smoothing in order to explain the key features seen in N-Body simulations. The CPDF ( $P(N)$ ) is obtained by differentiating  $P(> N)$ .

The leading contribution to the tail of the CPDF comes from the most massive haloes, as these haloes contribute the most to the volume above a given density. The contribution from low mass haloes brings in small variation in the CPDF due to the effect of smoothing, as compared to the CPDF for a single halo. This also implies that in our approach the relative forms of the non-Gaussian tail of the CPDF in real space and redshift space do not depend strongly on the power spectrum.

The lower panel of Figure 3 shows the probability distribution function for the  $n = -2$  power law model computed using the halo model and assuming a NFW profile in the limit of cell size much smaller than the virial radius of the most massive haloes. In this limit the CPDF computed from the halo model closely resembles the CPDF derived from a single halo shown in the top panel. In the following discussion, we shall compare these calculations with the CPDF in N-Body simulations.

There is a remarkable similarity in the distribution functions shown in Figure 2 and Figure 3. While the former is obtained from N-Body simulations, the latter is obtained from the halo model. The following assumptions have been used to compute the CPDF using the halo model.

- The density profile of haloes is universal (Navarro, Frenk, & White 1996).
- The 1D velocity dispersion  $\sigma$  does not vary with distance from the centre in a given halo.
- The cell size is much smaller than the virial radius of the most massive haloes.

We find that the halo model predicts a form for the tail of the CPDF that is remarkably similar to that seen in N-Body simulations.

It is noteworthy that the CPDF for the  $n = 0$  model in redshift space stays above the CPDF in real space over a much larger range of densities as compared to the CPDFs for  $n = -2$ . In the analysis given above, we pointed out that the tail of the CPDF computed using the halo model is dominated by the contribution from the most massive haloes. Therefore the relative behaviour of the CPDF in real and redshift space at high densities should have little dependence on the power spectrum as long as the three assumptions listed above are valid. We have used a cell size of 0.6 grid lengths for computing the CPDF from N-Body simulations, which is smaller than the typical radius of most massive haloes by a factor of 4 – 5 but not much more. Further, the most massive haloes for the  $n = -2$  model are much smaller than that for the  $n = 0$  model as we are able to probe higher non-linearities for the latter. This, in our view, is the reason for the differences seen in the two panels of Figure 2.

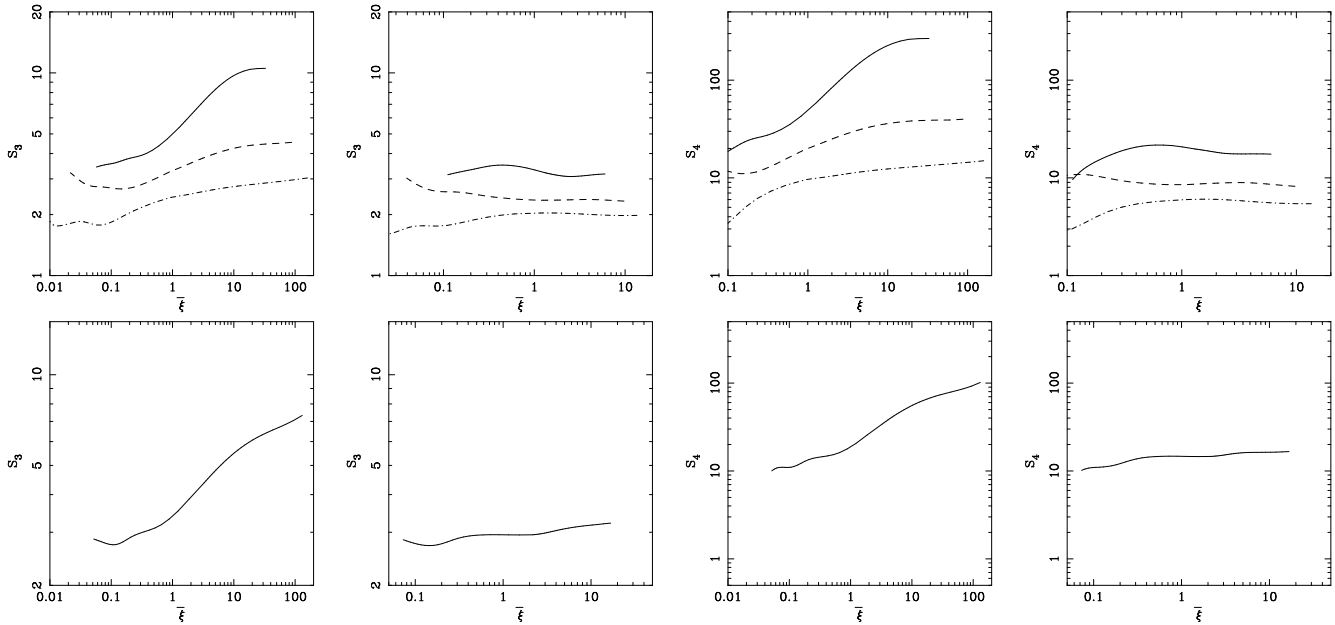


**Figure 4.** This figure shows  $S_3$  and  $S_4$  as a function of  $\bar{\xi}$ . The first column is for  $S_3$  in real space, and the second column is for redshift space. The third and fourth columns are for  $S_4$  in real and redshift space respectively. The top row is for power law models ( $n = 0, -1$  and  $-2$ ) and the lower panel is for  $\Lambda$ CDM at  $z = 0$ . In the top row, solid, dashed and dot-dashed lines correspond to power law models with indices  $n = -2, n = -1$  and  $n = 0$  respectively. Same scale is used for plotting the moments in real and redshift space to attract attention to the drastic reduction in spacing between the models in the non-linear regime.

### 3.2 Moments of Counts in Cells

The different shape of the high density tail of the CPDF in redshift space has implications for the moments of counts in cells. The rapid fall in the CPDF for the distribution in redshift space implies a much shorter non-Gaussian tail as compared to that in the real space. As the tail contributes significantly to higher moments, we expect the reduced moments to be much smaller in redshift space as compared to the real space. Figure 4 shows  $S_3$  and  $S_4$  as a function of  $\bar{\xi}$ . These have been plotted for three power law models ( $n = 0, -1$  and  $-2$ ) in the top panel and for the  $\Lambda$ CDM model in the lower panel. We have plotted these quantities in real space as well as redshift space. For ease of comparison, the panels showing moments for the redshift space and real space have been plotted with the same scale. Clearly, both the Skewness and Kurtosis are much smaller in redshift space as compared to the corresponding values in real space. For the power law model with  $n = -2$  and the  $\Lambda$ CDM model, the reduction in values is significant. As the tail of CPDF becomes more and more relevant at scales with a large amplitude of clustering (large  $\bar{\xi}$ ), the reduction is most significant at these scales. The ordering of values for  $S_n$  for various models is preserved in the mapping from real to redshift space, i.e., models with the larger  $S_n$  in real space also have a larger  $S_n$  in redshift space. This applies only to power law models as the  $\Lambda$ CDM model does not follow the ordering as we go from real to redshift space.

A noteworthy feature is that the values of  $S_n$  in redshift space show very little scale dependence at non-linear scales ( $\bar{\xi} \geq 1$ ). This again points to the finger-of-god effect as this effect is most significant at non-linear scales.

The significant reduction in the values of  $S_n$  in redshift space in the non-linear regime also results in reducing differences between different models. As galaxy distribution is observed in the redshift space, this implies that differentiating between variants of the  $\Lambda$ CDM model on the basis of higher moments is much more

difficult than would have been suspected on the basis of the expected values in real space.

In the regime of very small cell size, the differences in CPDF for different models arise mainly due to different mass functions. Therefore we expect the differences in the CPDF for different models in real space and redshift space to be of the same order, i.e., CPDF in real as well as redshift space should vary by a similar amount with the power spectrum. However the sharp fall off for the CPDF in redshift space reduces the range of densities over which the difference in CPDF contributes to the difference in moments. This, we believe, is the reason behind much smaller differences in Skewness, etc. for different models in redshift space as compared to the differences between the same models in real space.

Clustering properties of galaxies follow a pattern similar to clustering of highly over dense regions. Indeed, the generic evolution of galaxy correlation function can be deduced by studying correlation function of over dense regions (Bagla 1998b). Figure 5 shows  $S_3$  and  $S_4$  as a function of  $\bar{\xi}$  for particles in regions with  $\delta \geq 100$ . Here, the density contrast  $\delta$  is computed in real space and only particles in over dense regions with  $\delta \geq 100$  are retained. We study the clustering properties of these particles in real and redshift space and compute the two point correlation function and reduced moments. We have plotted  $S_3$  and  $S_4$  for the three power law models and the  $\Lambda$ CDM model in Figure 5. We see from the panels for real space that the moments are smaller for over dense regions as compared to the distribution of all the particles. Thus there are two reasons for reduction of moments in redshift space: bias and redshift space distortions. Figure 5 suggests that redshift space distortions are often the more dominant factor leading to reduction of Skewness, etc. At scales with  $\bar{\xi} \geq 1$  the reduced moments are almost constant; this feature is shared with the behaviour for the mass distribution. The non-Gaussian tail of the CPDF gets contribution mainly from very massive haloes, hence this is almost the same for

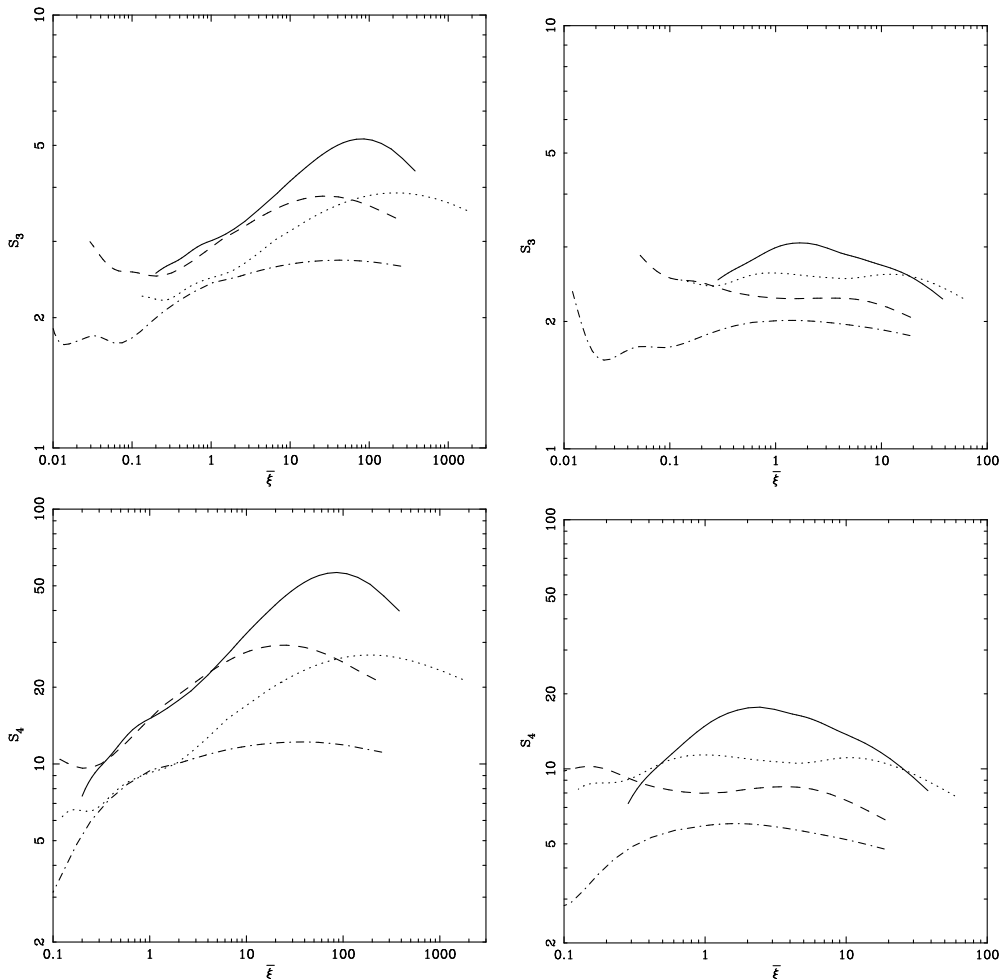


**Figure 5.**  $S_3$  (top row) and  $S_4$  (lower row) have been plotted as a function of  $\bar{\xi}$  for over dense regions (over density  $\delta \geq 100$ ) in real space and redshift space. In all the panels solid, dashed and dot-dashed lines correspond to power law models with indices  $n = -2$ ,  $n = -1$  and  $n = 0$  respectively. The dotted line corresponds to the  $\Lambda$ CDM model. The top left panel is for  $S_3$  in real space, the top right panel is for the same in redshift space. The lower left and right panels are for  $S_4$  in real and redshift space, respectively.

the full distribution and over dense regions. Therefore it is not surprising that the variation of Skewness, etc. with scales is almost the same for matter distribution and over dense regions. The variation of  $S_n$  with  $\bar{\xi}$  seen here is consistent with that seen for galaxies in the two degree field galaxy redshift survey (Croton et al. 2004). We are carrying out further analysis with models for occupation number in haloes in order to do a more quantitative comparison of models with the observed moments (Benson 2001; Tinker, Weinberg, & Zheng 2006).

#### 4 DISCUSSION

In this paper we have presented results of a study of the moments of counts of cells in real space as well as redshift space for power law models. These models are used to develop insights into the variation of the probability distribution function. We also use simulations of the  $\Lambda$ CDM model. We verify that in the weakly non-linear regime the Skewness and Kurtosis take on values calculated using perturbation theory. This is true in both the real and redshift space, though the finger-of-god effect leads to slightly smaller values in redshift space. We find that the values of higher moments like the

Skewness and the Kurtosis in the non-linear regime are very different in redshift space as compared to the corresponding values in real space. Higher moments are very sensitive to the non-Gaussian tail of the CPDF and we study that in order to understand the differences in values of moments in real and redshift space. We find that at highly non-linear scales, the tail of the CPDF in redshift space falls off very sharply much before the tail of CPDF in real space for the same model. This pattern is similar for different power spectra and we hypothesise that redshift space distortions (the finger-of-god effect) play a very important role in determining the form of the CPDF at small scales. We use the halo model to compute the form of the non-Gaussian tail of the CPDF in real and redshift space and find that we are able to reproduce the behaviour observed in N-Body simulations.

The rapid fall off of the CPDF in redshift space provides a natural explanation for the much smaller values of the Skewness and Kurtosis in the non-linear regime. Indeed, this also accounts for the much smaller differences in the values of reduced moments for different models.

We show that the above results carry over to the  $\Lambda$ CDM model as well. This indicates that at non-linear scales, higher moments



of the CPDF are relatively insensitive to the cosmological background.

We also study moments for highly over dense regions in order to estimate the effect of bias on Skewness, etc. In this case the moments in the non-linear regime take on smaller values as compared to the values for all the particles at the same scales. The reduction of moments in real space is related to the value of bias and can be modelled analytically in the weakly non-linear regime (Mo, Jing, & White 1997; Dekel & Lahav 1999). Thus there are two reasons for reduction of moments in the non-linear regime; whereas bias applies in both the real space and redshift space, redshift space distortions operate only in the latter. Figures 4 and 5 suggest that redshift space distortions are the stronger effect in almost all the cases.

We have shown that the halo model can be used successfully to model clustering in redshift space. This is very different from other approaches that have been employed for modelling the effect of redshift space distortions on clustering (Scoccimarro 2004). We propose to use this approach to model the three point correlation function, etc. in future studies.

## ACKNOWLEDGEMENTS

Numerical experiments for this study were carried out at the cluster computing facility in the Harish-Chandra Research Institute (<http://cluster.mri.ernet.in>). This research has made use of NASA's Astrophysics Data System.

## REFERENCES

- Bagla J. S., 1998a, MNRAS, 297, 251  
 Bagla J. S., 1998b, MNRAS, 299, 417  
 Bagla J. S., 2002, Journal of Astrophysics and Astronomy, 23, 185 (arXiv:astro-ph/9911025)  
 Bagla J. S., 2005, Current Science 88, 1088 (arXiv:astro-ph/0411043)  
 Bagla J. S., Padmanabhan T., 1994, MNRAS, 266, 227  
 Bagla J. S., Padmanabhan T., 1997a, MNRAS, 286, 1023  
 Bagla J. S. and Padmanabhan T. 1997b, Pramana – Journal of Physics 49, 161  
 Bagla J. S., Ray S., 2003, New Astronomy, 8, 665  
 Bagla J. S., Ray S., 2005, MNRAS, 358, 1076  
 Bagla J. S., Prasad J., 2006, arXiv:astro-ph/0601320  
 Bardeen J. M., Bond J. R., Kaiser N., Szalay A. S., 1986, ApJ, 304, 15  
 Benson A. J., 2001, MNRAS, 325, 1039  
 Bernardeau F., Colombi S., Gaztañaga E., Scoccimarro R., 2002, Physics Reports, 367, 1  
 Bertschinger E., Dekel A., 1989, ApJ, 336, L5  
 Bertschinger E., 1998, ARA&A, 36, 599  
 Binney J., 1977, ApJ, 215, 483  
 Brenier Y., Frisch U., Hénon M., Loeper G., Matarrese S., Mohayaee R., Sobolevskii A., 2003, MNRAS, 346, 501  
 Brainerd T. G., Scherrer R. J., Villumsen J. V., 1993, ApJ, 418, 570  
 Brainerd T. G., Villumsen J. V., 1994, ApJ, 431, 477  
 Branchini E., Eldar A., Nusser A., 2002, MNRAS, 335, 53  
 Buchert T., Dominguez A., 1998, A&A, 335, 395  
 Colombi S., Bouchet F. R., Schaeffer R., 1994, A&A, 281, 301  
 Colombi S., Bouchet F. R., Schaeffer R., 1995, ApJS, 96, 401  
 Colombi S., Bouchet F. R., Hernquist L., 1996, ApJ, 465, 14  
 Cooray A., Sheth R., 2002, PhR, 372, 1  
 Croft R. A. C., Gaztanaga E., 1997, MNRAS, 285, 793  
 Croton D. J., et al., 2004, MNRAS, 352, 1232  
 Davis M., Peebles P. J. E., 1977, ApJS, 34, 425  
 Dekel A., Bertschinger E., Faber S. M., 1990, ApJ, 364, 349  
 Dekel A., Lahav O., 1999, ApJ, 520, 24  
 Frisch U., Matarrese S., Mohayaee R., Sobolevski A., 2002, Natur, 417, 260  
 Fry J. N., 1996, ApJ, 461, L65  
 Gurbatov S. N., Saichev A. I., Shandarin S. F., 1989, MNRAS, 236, 385  
 Hamilton A. J. S., Kumar P., Lu E., Matthews A., 1991, ApJ, 374, L1  
 Hoyle F., 1953, ApJ, 118, 513  
 Hui L., Bertschinger E., 1996, ApJ, 471, 1  
 Hwang J., Noh H., 2005, astro, arXiv:astro-ph/0507159  
 Jain B., Mo H. J., White S. D. M., 1995, MNRAS, 276, L25  
 Jones B. J., Martínez V. J., Saar E., Trimble V., 2005, RvMP, 76, 1211  
 Kaiser N., 1984, ApJ, 284, L9  
 Kaiser N., 1987, MNRAS, 227, 1  
 Kanekar N., 2000, ApJ, 531, 17  
 Ma C., 1998, ApJL, 508, L5  
 Matarrese S., Lucchin F., Moscardini L., Saez D., 1992, MNRAS, 259, 437  
 Matsubara T., 1994, ApJ, 424, 30  
 Matarrese S., Coles P., Lucchin F., Moscardini L., 1997, MNRAS, 286, 115  
 Mo H. J., White S. D. M., 1996, MNRAS, 282, 347  
 Mo H. J., Jing Y. P., White S. D. M., 1997, MNRAS, 284, 189  
 Mohayaee R., Frisch U., Matarrese S., Sobolevskii A., 2003, A&A, 406, 393  
 Mohayaee R., Tully B., Frisch U., 2004, arXiv:astro-ph/0410063  
 Monaco P., Efstathiou G., 1999, MNRAS, 308, 763  
 Narayanan V. K., Weinberg D. H., 1998, ApJ, 508, 440  
 Narayanan V. K., Croft R. A. C., 1999, ApJ, 515, 471  
 Navarro J. F., Frenk C. S., White S. D. M., 1996, ApJ 462, 563  
 Nityananda R., Padmanabhan T., 1994, MNRAS, 271, 976  
 Nusser A., Dekel A., 1992, ApJ, 391, 443  
 Padmanabhan T., 1996, MNRAS, 278, L29  
 Padmanabhan T., Cen R., Ostriker J. P., Summers F. J., 1996, ApJ, 466, 604  
 Padmanabhan T., 2002, Theoretical Astrophysics, Volume III: Galaxies and Cosmology. Cambridge University Press.  
 Peacock J. A., Dodds S. J., 1996, MNRAS, 280, L19  
 Peacock J. A., 1999, Cosmological physics. Cambridge University Press.  
 Peebles P. J. E., 1974, A&A, 32, 391  
 Peebles P. J. E., 1980, The large-scale structure of the universe. Princeton University Press, Princeton.  
 Peebles P. J. E., 1985, ApJ, 297, 350  
 Ray S., Bagla J. S., 2004, astro-ph/0405220  
 Rees M. J., Ostriker J. P., 1977, MNRAS, 179, 541  
 Roukema B. F., Valls-Gabaud D., Mobasher B., Bajtlik S., 1999, MNRAS, 305, 151  
 Sahni V., Coles P., 1995, PhR, 262, 1  
 Scoccimarro R., 2004, PhRvD, 70, 083007  
 Seljak U., 2001, MNRAS, 325, 1359  
 Shandarin S. F., Zeldovich Y. B., 1989, RvMP, 61, 185  
 Sheth R. K., Tormen G., 2004, MNRAS, 350, 1385  
 Sheth R. K., Mo H. J., Tormen G., 2001, MNRAS, 323, 1

- Silk J., 1977, ApJ, 211, 638  
Smith R. E., et al., 2003, MNRAS, 341, 1311  
Springel V., Yoshida N., White S. D. M., 2001, NewA, 6, 79  
Taruya A., Hamana T., Kayo I., 2003, MNRAS, 339, 495  
Taylor A., Valentine H., 1999, MNRAS, 306, 491  
Taylor A. N., Watts P. I. R., 2000, MNRAS, 314, 92  
Tegmark M., Peebles P. J. E., 1998, ApJ, 500, L79  
Tinker J. L., Weinberg D. H., Zheng Z., 2006, MNRAS, 368, 85  
Watts P. I. R., Taylor A. N., 2001, MNRAS, 320, 139  
Weinberg D. H., 1992, MNRAS, 254, 315  
White M., 2001, MNRAS, 321, 1  
Whiting A. B., 2000, ApJ, 533, 50  
Zel'Dovich Y. B., 1970, A&A, 5, 84